EES Batteries

PAPER

View Article Online
View Journal

Cite this: DOI: 10.1039/d5eb00196j

Vertically orientated one-dimensional titania lepidocrocite quasi nanoflakes for stabilized lithium deposition in lithium metal anodes

Neal A. Cardoza,[a,c] Mary Qin. Hassig,[b] Tran Ngo,[c] Taber Yim,[a,c] Brianna Markunas,[a] Joshua Snyder,[a] Michel W. Barsoum[b] and Vibha Kalra*[c]

Lithium metal has long been considered the ideal anode for a variety of cell chemistries owing to its quite high gravimetric capacity. Dendrite growth, loss of Li in SEI, and processing challenges, however, restrict its practical deployment. Here, a new form of titania, TiO_2, *viz*. 1-dimensional lepidocrocite (1DL) are used as the basis for creating a Li scaffold. The basic units are Ti–O chains – 5 × 7 Å^2 in cross-section – that can assemble into quasi 2D nanoflakes. These nanoflakes are synthesized *via* a bottom-up reaction, directly from commercial 3D-bulk solids at near ambient temperatures and pressures. Here the 2D flakes are vertically oriented to guide Li-metal deposition and serve as a Li metal scaffold. This is achieved through a directional control freezing of an aqueous blade cast slurry. The vertical-1DLs (V-1DL) enable Li nucleation at lower overpotentials compared with bare copper or a conventional cast slurry of 1DL. Their long-range order and vertical alignment contribute to improved Li-ion fluxes. V-1DLs also show improved cyclability with plating and stripping at 2 mAh cm^{-2} and 2 mA cm^{-2}, up to 150 h. Dead Li measurements further indicate that V-1DL reduces Li loss to dead Li.

Received 12th October 2025,
Accepted 6th February 2026

DOI: 10.1039/d5eb00196j

rsc.li/EESBatteries

Broader context

To meet growing demand for higher energy density, the field is shifting from lithium-ion batteries (LIBs) to lithium-metal batteries with a low redox potential (−3.04 V *versus* standard hydrogen electrolyte, SHE) and high theoretical capacity (3860 mAh g^{-1}). However, dendritic Li growth, dead Li accumulation, and large volume changes leading to safety concerns remain major barriers to large-scale application of Li metal batteries. Moreover, Li production emits 15 tons of CO_2 per ton of Li produced, posing environmental concerns for the battery industry. In light of this, research has been devoted to anode-free Li metal batteries (AFLMBs), which offer high volumetric and gravimetric energy density, reduced Li consumption leading to decreased volume, weight, and complexity during manufacture, and enhanced safety by eliminating excess Li. Yet, the absence of Li^+ host material makes AFLMBs susceptible to dendritic Li, irreversible solid electrolyte interphase (SEI) growth, and depletion of active Li. Therefore, in this study, we developed a 3D low tortuosity current collector with vertically aligned lepidocrocite nanofilaments that guides Li deposition, reduces Li nucleation overpotential, suppresses dendrites and enhances Li plating and stripping thereby prolonging cycle life. This simple, scalable, and environmentally benign strategy paves the way toward large-scale, safe, and high energy density AFLMBs that can advance next-generation energy storage technologies.

1. Introduction

The rapid development and demand for electric vehicles, and the electrification of other systems, have driven the demand for energy storage with high specific energy densities. Currently, lithium-ion (Li-ion) batteries are being used to meet some of this demand.[1,2] However, for more energy-dense systems, lithium metal (Li) anode systems are best suited to meet the ever-increasing demand, as Li has a quite high specific capacity of 3860 mAh g^{-1} and a low electrochemical potential of −3.04 V *vs.* SHE.[3,4] Li metal anodes are the ideal anode for new next generation chemistries like lithium sulfur.[5–7] However, there are well documented challenges that limit their practical application.

Li metal is highly reactive and as such suffers from dendrite and dead Li formation. Uneven deposition of Li across the surface of the electrode leads to the formation of Li dendrites that can eventually pierce the separator and lead to short-circuits.[4,8] Additionally, Li's reactivity with the electrolyte leads to the formation of a solid electrolyte interface (SEI). Over the course of cycling and formation of dendrites, this interface

[a]*Department of Chemical and Biological Engineering, Drexel University, 3141 Chestnut Street, Philadelphia, PA-19104, USA*
[b]*Department of Materials Science Engineering, Drexel University, 3141 Chestnut Street, Philadelphia, PA-19104, USA*
[c]*Robert Frederick Smith School of Chemical and Biomolecular Engineering, Cornell University, Ithaca, NY-14853, USA. E-mail: vk69@cornell.edu*

breaks down. The subsequent rebuilding of the SEI consumes Li, electrolyte, and traps Li in the SEI. This trapped Li is called dead Li, as it is electrochemically inactive.[9–11] These issues lead to the loss of Li, short-circuits, and poor cycle life. In recent years many strategies have been developed to mitigates the drawbacks of Li, focusing on the electrolyte, charging mechanisms, coatings and current collector modifications.[12–22]

Current collector modifications and coatings have attracted a lot of interest, as improving the substrate of the electrodeposition, improves the overall cyclability through better uniform dense Li deposition. Considering Cu is non-lithiophilic, a variety of elements alloyed with Cu (Ag, Zn, Au, Sn, and Sb) improve its lithiophilicity.[23] For instance, Li *et al.* evaporated Sn on Cu under vacuum to create a lithiophilic nanolayer, demonstrating 40% reduction in nucleating voltage.[24] However, many of these alloys primarily improve nucleated Li but do not homogenize the Li ion flux. Artificial coatings such as multilayer graphene and polyethylene oxide on Cu can improve the homogeneity of Li surface flux.[20,21] We have additionally shown how a facile film of poly(vinylidene fluoride) can improve Li ion flux aided with Li salts.[7] However, these coatings can separate through the volume expansion of the Li plated on the surfaces, ultimately increasing the energy required for Li nucleation.

To combat these issues, 3D current collectors have been proposed to improve flux homogeneity. This is typically carried out by changing the morphology of the current collector, such as Cu mesh by growing vertically aligned fibers such as carbon nanofibers.[25,26] The 3D morphology improves the Li flux homogeneity, lowers nucleation overpotential, and suppress dendritic growth. Yet, dopants are needed to further make the 3D structure lithiophilic and contribute to the SEI.

TiO_2 has gained popularity as a Li metal host, owing to its affinity for Li and electrochemical stability. Additionally, Li can be stored in the lattice of TiO_2 with low volume expansion of ~4%.[27–29] Typically, the TiO_2 used for such purposes is anatase and is further doped with lithiophilic atoms like silver.[30–33] As far as we can ascertain, lepidocrocite TiO_2 has not been used as a Li metal host. However, lepidocrocite TiO_2 has been used in numerous reports as a layered anode intercalating Li^+, owing to its layered structure.[34–36] This inherent layered crystal structure can be leveraged to increase the lithiophilicity of the TiO_2. Furthermore, applications of lepidocrocite TiO_2 have primarily relied on sol–gel approaches with titanium isopropoxide, leading to a complicated synthesis pathway.

Herein, we introduce a new class of nanomaterials, 1-dimensional lepidocrocite nanofilaments (1DLs) vertically aligned on Cu. These 1DLs–TiO_2 nanofilaments are synthesized through a process we recently developed by reacting earth-abundant, nontoxic, Ti-containing precursors with quaternary ammonium hydroxides at ~80 °C and 1 atm for 3–5 days. The cross section of these filaments falls within the 5 × 8 $Å^2$ range. Thus far, we have demonstrated a wide application range of the 1DL materials, including Li–S storage, hydrogen production, electrocatalytic oxygen evolution, dye degradation, and water purification.[37–41] This material is inherently lithiophilic and can additionally intercalate Li ions between its layers. Additionally, the hydroxyl surface functionalization of these material further contributes to an SEI with a higher concentration of LiOH.[42,43] Furthermore, we demonstrate their electrochemical performance as a planar structure, isolating the effect of 3D morphology from the intrinsic properties of 1DLs as Li metal hosts.

2. Results

1DLs have shown a range of applications arising from their high surface area, hydroxyl functionalization, lithiophilicity, and ability to intercalate Li. To study the role of 1DL as a Li host, two electrode classes were fabricated: the first being 3-D vertical-1DL called V-1DL and the second being the more traditional, planar, horizontal-1DL called H-1DL.

Fig. 1A shows the directional freeze-casting process used to create V-1DL. A cast aqueous slurry is frozen from the bottom up, enabling the formation of vertical ice crystals growing from the Cu surface. These vertical ice crystals orient the 1DLs perpendicular to the surface, after sublimation, V-1DL is obtained.

Typical SEM micrographs are shown in Fig. 1B–D. In Fig. 1C, the width between the nanoflake arrays is ~20 μm, and the dry thickness is ~40 μm, seen in Fig. 1D. Expanded SEM images, shown in Fig. S1, illustrate V-1DL structure. The elemental mapping of V-1DL is presented in Fig. S2, where 1DL contributes to the Ti and O signals, the carbon black contributes to the C signal and the polymer binder contributes to the C and O signals. Lastly, the vertical orientation is confirmed in the EDS maps (Fig. S2) where the Cu signal appears in lines where there are no Ti signals.

The 3D structure of the current collector is shown to provide inherent benefits for the overall deposition of Li on the surface of the 2D electrodes, which arises from the improvement in the homogenization of the Li ion flux on the surface of the electrode.[44–46] V-1DL compared to H-1DL benefits from low tortuosity and the easy access of Li to the deposition channels between the 1DL nanoflakes. The higher tortuosity structure of H-1DL can be seen the SEM images seen in Fig. S3. Additionally, the lithiophilicity of the 1DL increases the benefit of the low tortuosity of Li-ion channels. Furthermore, 1DL initially intercalates Li into the layered lepidocrocite structure, enabling the Li to nucleate and directly on the nanoflakes. Lastly, the 3D nature of V-1DL increases the overall effective surface area for the deposition of the lithium, lowering the local current density near the surface of V-1DL when compared to 2D electrodes resulting in larger Li nuclei and even deposition of Li on the electrode surface.[48] This larger Li nuclei results in more evenly plated Li layer, improving the cyclability.

Galvanostatic Li plating overpotentials and Tafel exchange current densities, shown in Fig. 2A and B, respectively, were used to shed light on the Li deposition process. Three electro-

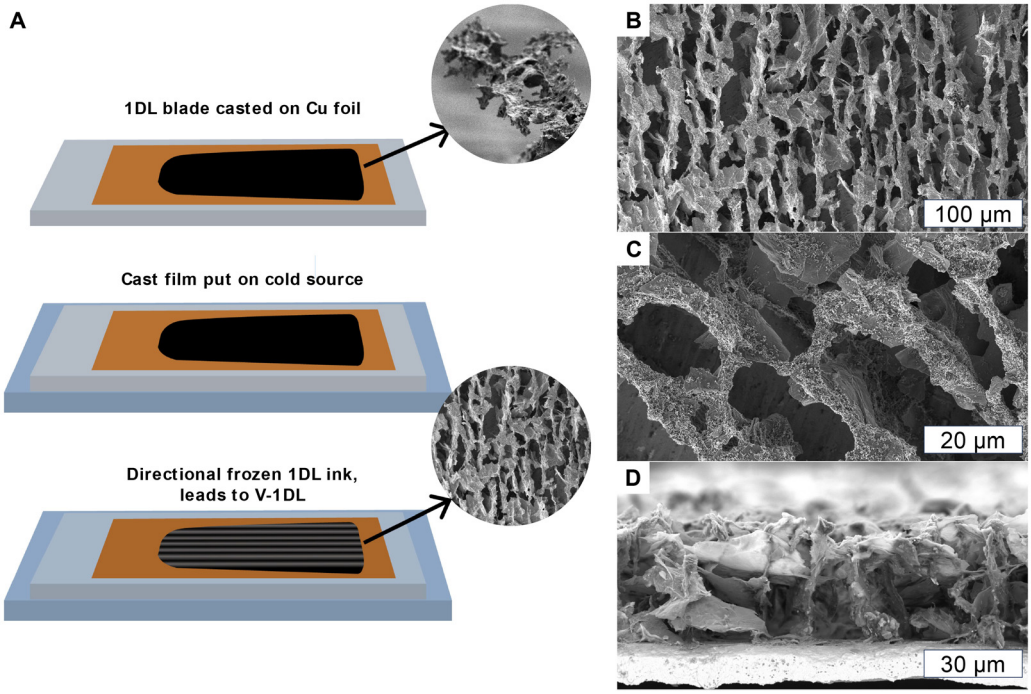

Fig. 1 Schematic of directional freezing and casting of V-1DL in panel A. SEM images of the top-down view of V-1DL after freeze drying, demonstrating the vertical array of 1DL, seen in Panel B and C. The cross-section view of V-1DL seen in panel D.

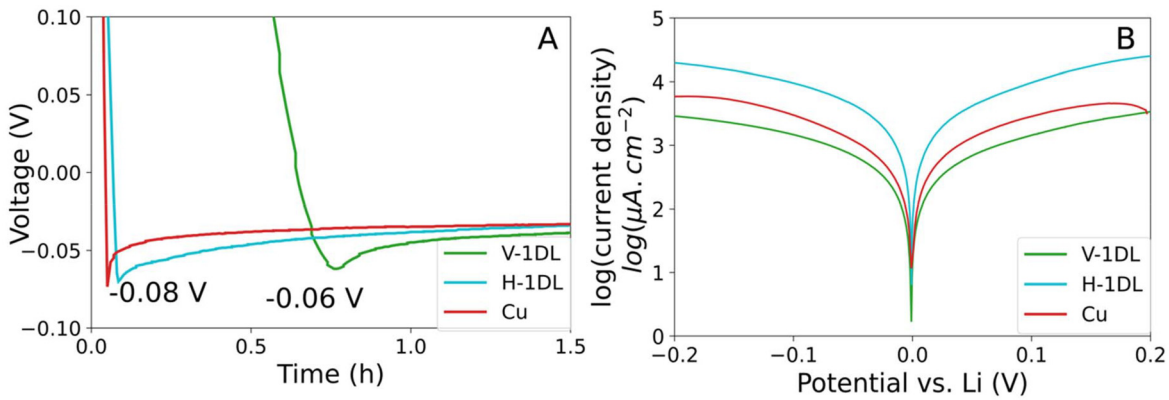

Fig. 2 (A) Overpotential of Li plating on various substrates at 0.25 mA cm^{-2} (B) Tafel plots of electroplated Li on various substrates, showing lower exchange current density of V-1DL.

des were tested: Cu, H-1Dl and V-1DL. The initial voltage drop of nucleating Li on the surface of the electrode of the former two are more dramatic (−0.08 V *vs.* Li/Li^+) than that on V-1DL (−0.06 V *vs.* Li/Li^+). The nucleation overpotential of Cu (−0.029 V) is higher than H-1DL (~0.024 V) and ~0.017 V for V-1DL. These overpotentials are inversely related to the size of the Li nuclei.[49] It has also been shown that larger Li nuclei contribute to lower dendritic Li growth.

However, V-1DL structure contributes to the homogenization of Li ion flux resulting in even distribution with larger nuclei of Li. Additionally, surface Li deposition can be characterized by the limiting exchange current densities derived from the Tafel plot seen in Fig. 2B. All exchange currents are normalized to the geometric area of the electrodes. Thanks to its layered structure with various Ti^{4+} vacancies and surface hydroxyl groups, lepidocrocite TiO_2 could promote Li^+ intercalation by providing low-energy diffusion pathways within its interlayers and vacancies, thus facilitating fast Li^+ diffusion and interfacial ion transfer kinetics.[34] This intrinsic chemistry of 1DL was reflected in Fig. 2A where both H-1DL and V-1DL display lower overpotentials than Cu. Although lower overpotential is often associated with reduced exchange current density, the higher exchange current density of H-1DL compared to Cu arises from the normalization by the geometric

area rather than the electrochemically surface area.[50] However, owing to a significantly large effective surface area, V-1DL still shows the lowest exchange current density among the three electrodes (Fig. 2B). A lower limiting exchange current density can be directly related to the nuclei size of the lithium deposition and allowable rate of Li deposition. Here, the lower limiting exchange current density is achieved largely through a higher effective surface area of V-1DL. It has been shown that a lower limiting exchange current density is characteristic of a denser and more even Li deposition. Thereby, this demonstrates that a denser Li layer with reduced dendritic Li growth forms during the initial plating of Li on the surface of V-1DL when compared to 2D electrodes, ultimately contributing to better cyclability of Li metal anodes. For a more quantitative correlation between nucleus density and overpotential, potentiostatic nucleation transients were performed on bare Cu and V-1DL (Fig. S7). Despite some deviations from the theoretical Scharifker-Hills nucleation model due to its complicated 3D structure and the simultaneous SEI formation and electrolyte decomposition in the Li plating process, V-1DL shows a better fit to the 3D instantaneous nucleation model which was reported to yield more uniform and homogeneous nucleation growth compared to the 3D progressive mechanism observed in Cu.[51] Based on the fitted nucleation model, nuclei densities were calculated for Cu and V-1DL, in which a noticeably lower value was obtained in V-1DL, suggesting that V-1DL is more effective in decreasing nucleation overpotential as the nuclei number density increases with the cube of the overpotential (Table S2).[49,52,53]

The cyclability of the Li metal anodes were evaluated through galvanostatic stripping and plating cycling of symmetric cells. Li was first plated from a half cell with a Li metal foil and with working electrode being V-1DL, H-1DL, or Cu. The now plated Li electrodes from two half cells were then assembled into one symmetric cell. These symmetric cells were tested at 2 mAh cm^{-2} and 2 mA cm^{-2} for all three electrodes. V-1DL electrode was additionally tested at 1 mAh cm^{-2} and 1 mA cm^{-2}, as shown in Fig. 3A. Fig. 3B and C show the cycling result for the three electrodes at 2 mAh cm^{-2} and 2 mA cm^{-2}. In Fig. 3B, the cycling of Cu starts to fail as early as 40 h, with complete failure occurring at 90 h. This can be largely attributed to the formation of increased dendritic Li, and increasing accumulation of dead Li. At 40 h, V-1DL and H-1DL show lower polarization and better stripping and plating of Li seen in Fig. 3C. At 40 h of cycling, H-1DL indicates a lower polarization than even V-1DL which can be explained by the plating of Li on the surface of the electrode.

However, once this plated Li is consumed through SEI formation and dead Li accumulation, it is reasonable to conclude that the tortuous structure of H-1DL leads to its failure. Nevertheless, compared to Cu, H-1DL demonstrated longer cyclability, attributed to the better SEI components generated through presumably the hydroxyl functionalization of the 1DL, as Cu and H-1DL share a similar planar morphology. Introducing the added benefits of the low 3D tortuosity of V-1DL further improves the cyclability from 110 h to over 150 h for cells cycled at 2 mAh cm^{-2} and 2 mA cm^{-2} (Fig. 3B). At the lower cycling rate, V-1DL electrode remained stable for more

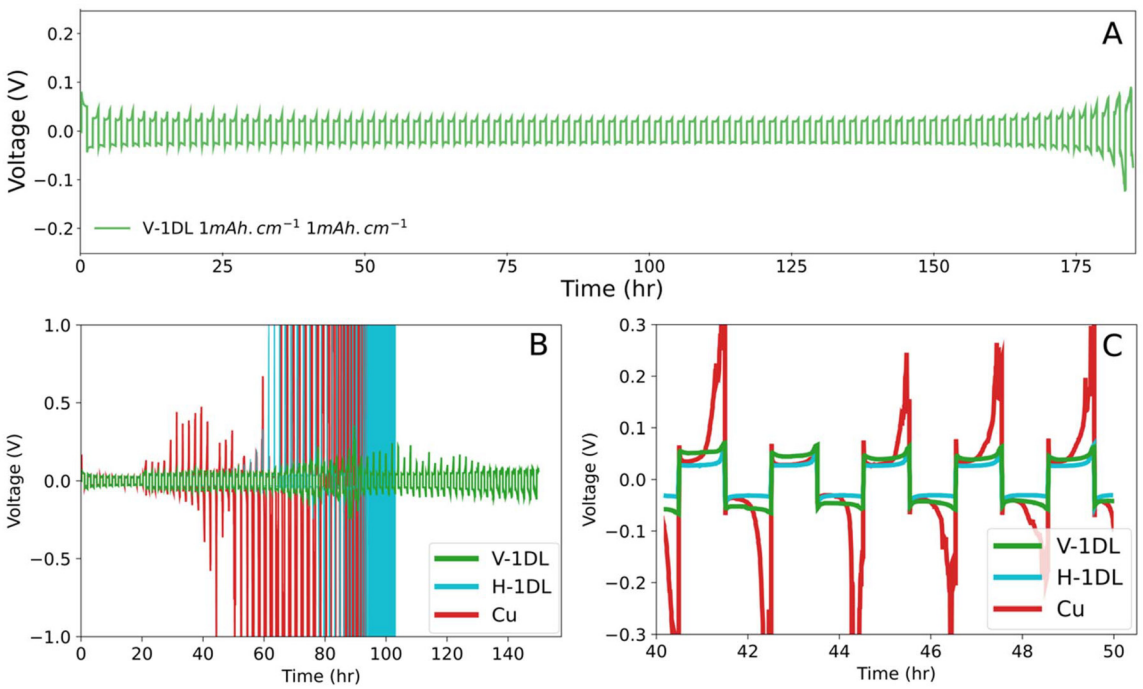

Fig. 3 Electrochemical Cycling of plated Li on V-1DL, H-1DL, and Cu as symmetric cells. (A) Symmetric cell of V-1DL running at 1 mAh cm^{-2} and 1 mA cm^{-2}, (B) symmetric cells run at 2 mAh cm^{-2} and 2 mA cm^{-2}, (C) zoomed in voltage profile of symmetric cells cycled at 2 mAh cm^{-2} and 2 mA cm^{-2}, showing Cu starting to fail at 40 h.

than 170 h (Fig. 3A), demonstrating the overall improved cyclability of V-1DL owing to its 3D low tortuosity, homogenous Li-ion flux, and improved SEI formation. Nevertheless, some polarizations were still observed in V-1DL at higher cycling rate (Fig. 3B). This is likely due to interfacial degradation under more aggressive Li plating/stripping conditions. In addition, the side reactions between residual water that has not been removed during drying and Li could likely cause the loss of inventory Li. While V-1DL provides a significant advantage over bare Cu and H-1DL, this test highlights the extreme challenges of AFLMBs operating at high current density and areal capacity.

The improved cyclability can be also understood by imaging the anodes post Li plating, *via* SEM seen in Fig. 4. Two Li half cells were made for each electrode, the first being Li plated for 4.5 mAh (left and center columns in Fig. 4) and the second to 9 mAh (right column in Fig. 4). It is evident from Fig. 4A and B that there is dendrite-like whisker plating occurs on Cu. This dendrite plating leads to uneven Li deposition, as seen in Fig. 4C, leading to uneven stripping and plating in subsequent cycles.

This type of uneven deposition contrasts with Li deposited on H-1DL and V-1DL, as shown in Fig. 4D. Here, Li is plated into H-1DL structure, which due to its high tortuosity, resulting in uneven stripping and plating of Li, leading to dendrites during cycling. However, the Li plated in H-1DL is smooth in localized areas on the electrode surface, as seen in Fig. 4F, though overall Li deposition at the electrode level remains uneven.

Lastly, for V-1DL at 4.5 mAh of plated Li, the Li is deposited both on the surface of the Cu in between the nanoflakes and nucleates on the nanoflakes themselves, as seen in Fig. 4G and H. At the full 9 mAh of Li plated on the surface of V-1DL in Fig. 4I, there is a qualitatively more even surface layer of Li deposited on the surface compared to lower capacities. While

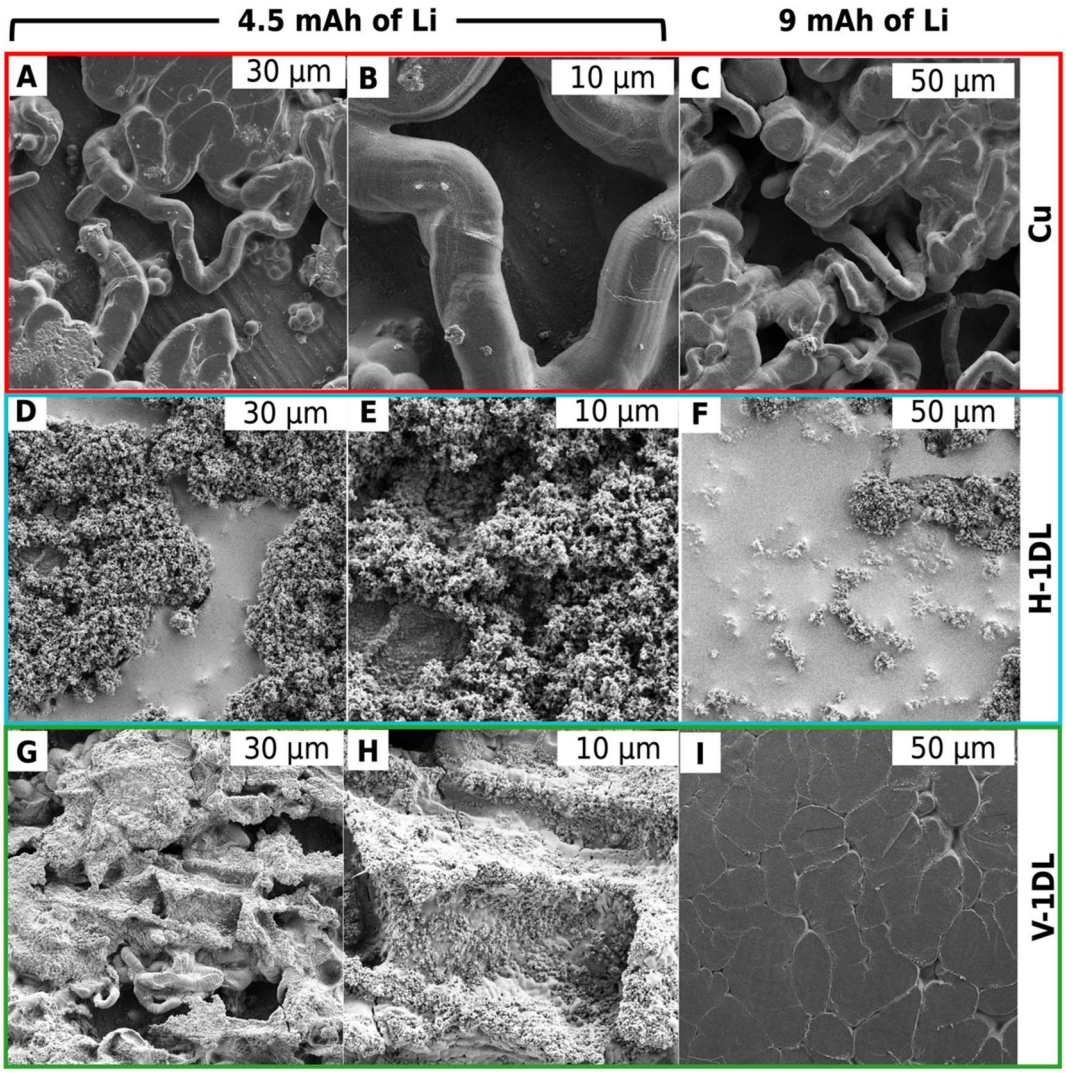

Fig. 4 Postmortem SEM top-down micrographs of Li plated on (A–C) Cu, (D–F) H-1DL, and (G–I) V-1DL, indicating the morphology of the deposited of Li at two different Li deposition amounts.

these observations are based on a limited number of fields-of-view counts, the types of initial Li deposition seen on the surface of Cu, H-1DL and V-1DL are consistent with the differences in the overall cyclability of the electrodes.

To further understand how the proportion of Li lost to dead Li is affected by the 1DLs and electrode design, the cycled electrode had their dead Li measured through titration gas analysis, gaining insight into the SEI *via* the proportion of irreversible and reversible Li plating during cycling. The experimental setup, seen in Fig. 5A (created with BioRender.com, N. Cardoza, 2026 [60]), is a modified version from Fang *et al.*[54] The modification arises from the direct correlation of hydrogen, H_2, measured *versus* a pre-measured amount of Li reacted with DI water. The calibration curve, as seen in Fig. S4, establishes a relationship between Li weight and the H_2 integrated area. It is clear from Fig. 5B that Cu, despite having higher reversible Li plated, has a significant amount of Li lost to dead Li compared to H-1DL and V-1DL electrodes. The proportion of Li lost to SEI elements, while higher in V-1DL and H-1DL owing to the increased effective surface areas, is more stable than planar, as indicated by the symmetric cell cycling. The continual loss of Li to SEI and dead Li in Cu leads to a loss of Li and cyclability.

We then obtained postmortem XPS depth profiles on cycled electrodes to further understand the role of SEI on these electrodes, specifically the differences between the SEI on Cu and V-1DL samples. These electrodes were plated with Li and then

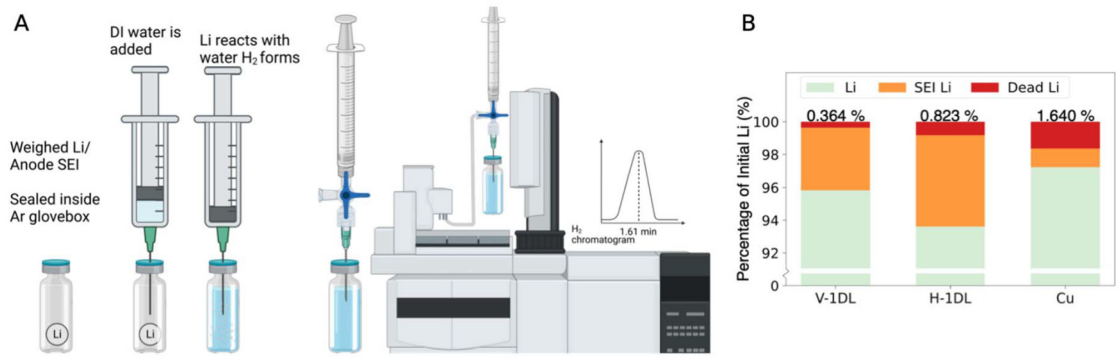

Fig. 5 Dead Li titration gas chromatography, experimental schematic in A [60] and the Li lost breakdown based on dead Li analysis in B.

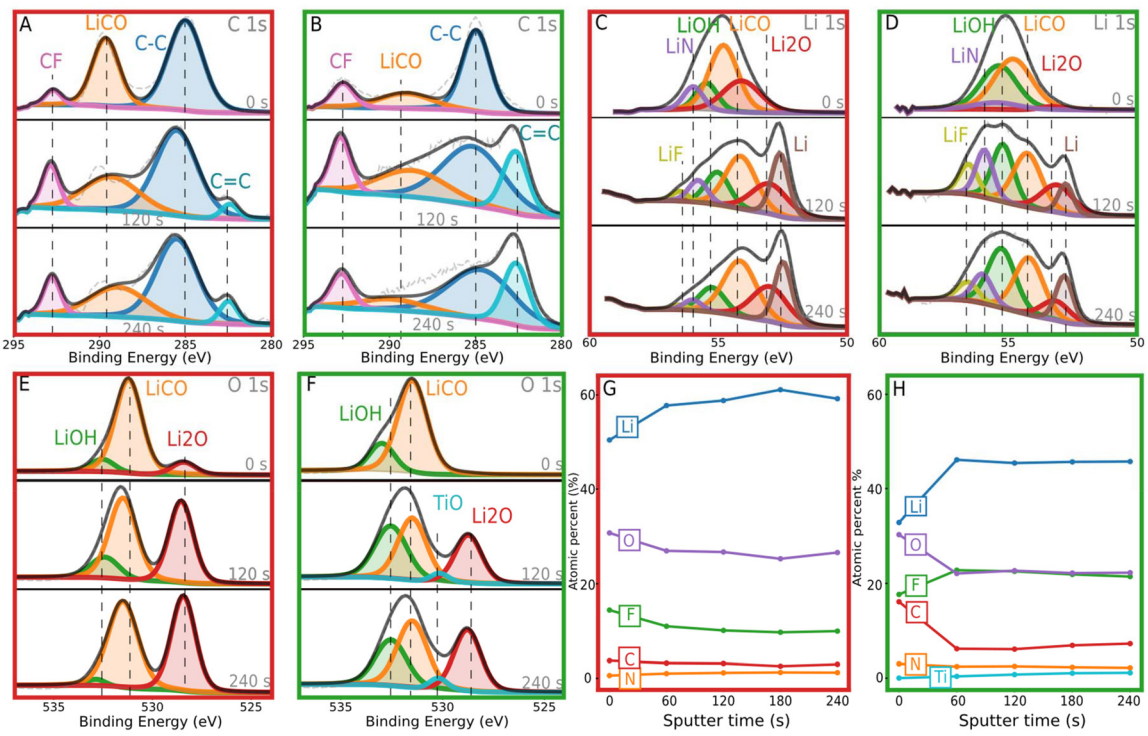

Fig. 6 Postmortem XPS spectra of cycled electrodes collected after different levels of sputtering, Cu in red and V-1DL in green. (A) Cu C 1s, (C) Cu Li 1s, (E) Cu O 1s, (G) Cu atomic percentage of elements, (B) V-1DL C 1s, (D) V-1DL Li 1s, (F) V-1DL O 1s, and (H) V-1DL atomic percentage of elements.

cycled 10 times at 2 mAh cm^{-2} and 2 mA cm^{-2}. The cycled electrodes were then removed from the cell and transferred *via* an Ar transfer cell into the XPS chamber. The samples were sputtered with an Ar gun for 60 s per sputter, for a total of 4 rounds of sputtering. The XPS spectra for C 1s, Li 1s, O 1s, and atomic percentages are seen in Fig. 6, where the red border refers to Cu and the green to V-1DL. N 1s and F 1s spectra are reproduced in Fig. S5 with fitting constraints in Table S1.

When the Cu and V-1DL electrode XPS spectra are compared, the latter shows increased lithium hydroxide (LiOH), N, and F which can be attributed to a more robust SEI.[55–57] LiOH and Li_3N have increased ionic conductivity when compared to lithium carbonate (Li_2CO_3).[58] The increased LiOH concentration is seen in Fig. 6E and F for O 1s, and additionally in 6C and 6D for Li 1s, for V-1DL compared to Cu. LiOH, shown in green, appears as a peak with binding energy (BE), of 532.5 eV for O 1s and 55.3 eV in Li 1s. Cu demonstrates a higher proportion of Li_2CO_3, seen in orange, at 288.9 eV in C 1s, 54.2 eV in Li 1s, and 531.4 eV in O 1s. It is important to note that these compounds have quite similar binding energies. Despite this, it is evident from the C 1s spectra in Fig. 6A and B that Cu has a greater proportion of Li_2CO_3 when compared to V-1DL. It has been shown that having a higher concentration of Li_2CO_3 in the SEI can contribute to poor cyclability.[47] Additionally, seen in the atomic percentages in Fig. 6G, the atomic percent of F and N increase for V-1DL electrode as the sample was sputtered. For the Cu electrode, the atomic percent of F and N decrease and plateau the further the sample was sputtered (Fig. 6G).

3. Conclusion

Herein, we have expanded on the role of 1DL in lithium metal cells, building on our prior work with 1DLs as sulfur hosts in Li–S batteries. Additionally, utilizing the nanoflake morphology of the 1DL, we demonstrated its role in a low tortuosity, lithiophilic material with vertical channels as a Li metal host. The vertical channels were constructed through directional freezing of an aqueous slurry, consisting of 1DL nanoflakes, carbon black, and sodium methyl cellulose. The design of this electrode offers reduced Li nucleation overpotential and improved plating and stripping compared to planar Cu and H-1DL. However, H-1DL without the vertical morphology on the electrode offers improved plating and stripping cycling when compared to similarly planar Cu, indicating the role of 1DL. The Li deposition was further investigated with post-mortem SEM to understand the morphology of the plated Li, where planar Cu had uneven Li plating and dendritic Li, compared to V-1DL with even surface of plated Li. TGC was further used to quantify the proportion of dead Li and SEI Li within the irreversible Li. TGC indicated that while Cu had the highest reversible Li plated at 10 cycles, it had the most Li lost to dead Li. In contrast, V-1DL had the lowest dead Li, owing to the 1DL hydroxyl functionalization and the 3D low tortuosity structure. Additionally, post-mortem XPS of these cycled electrodes show the formation of more F and N species when compared to Cu. Furthermore, Cu shows the formation of a higher degree of Li_2CO_3 compared to a higher degree of lithium hydroxide in 1DL, which could explain the more robust SEI of 1DL. These results indicate that V-1DL can be used as a Li host material.

4. Experimental

4.1. 1DLs synthesis

The methods to make the 1DL have been previously described in our previous papers.[39,40,59] Briefly, 10 g of TiB_2 powders (purity, 99+% metal basis, Alfa Aesar, USA) were mixed with 100 ml of tetramethyl ammonium hydroxide (TMAOH) at 80 °C for 4 days, in a polyethylene bottle into which 2 needles were inserted to prevent pressure buildup. After reaction, the mixture was washed with 200 proof ethanol (Decon Labs) until a neutral pH was reached. After which, the 1DL NFs were separated from unreacted TiB_2 using a DI water wash and a centrifuge run at 3500 rpm for 30 minutes to form a colloidal suspension. The latter was then mixed with 5M lithium chloride (LiCl) in an aqueous solution (Thermo Scientific Chemicals 99% anhydrous) at ~2× the volume of the colloidal suspension, on a stir plate overnight for ~20 h. The excess LiCl was then washed with DI water till a neutral pH was again reached. The final 1DL water mixture was then centrifuged to separate the 1DLs from excess water and the aqueous supernatant was discarded. The sediment that was separated, consisting of 1DL with residual water was then freeze dried with liquid N_2 overnight and used as is.

4.2. Fabrication of vertical 1DL morphology

The 1DL NFs were orientated vertically using directional freezing of a slurry. To make the slurry, 1DL NFs were mixed with carbon black (Alfa Aesar) and sodium carboxymethyl cellulose (Frontier Scientific) in a mass ratio of 50 : 20 : 30 with 1.5 ml of DI water, in a Thinky planetary mixer. This was then cast on a Cu foil on a steel plate with doctor blade at a thickness of 75 μm (top schematic in Fig. 1A) The cast slurry on the steel plate was directionally frozen from below? With a larger thermal sink acting as a cold plate (seen as blue-grey plate in bottom schematic of Fig. 1A) at −196 °C using liquid N_2. After which, the anode was subjected to vacuum for 24 h, allowing the ice to sublimate *via* freeze drying.

4.3. Building the coin cells

For electrochemical testing, electrodes were punched in 11 mm disks and assembled into stainless steel coin cells (MTI, China) and (TMXCN, China). First, they were transferred into the glovebox (Mbraun, Germany) with H_2O and O_2 levels <1 ppm. After which an initial Li layer was deposited on the electrodes by building half-cells with Li counter and reference electrodes. 20 μL of the electrolyte (1 : 1 dimethoxyethane :

dioxolane, 1 M lithium bis(trifluoromethanesulfonyl)imide, 1 wt% of lithium nitrate) (Gotion USA) was used, and a 15 mm disk of Celgard 2325. Li was then deposited on the electrode galvanostatically at 0.25 mA for 36 h on Neware cyclers. After which the coin cells were decrimped and the electrodes were harvested to be used in a symmetric cell. The symmetric cell was built similarly, with identical electrodes on either side of the Celgard 2325 separator with 20 μL of the same electrolyte from Gotion USA.

4.4. Electrochemical tests

All galvanostatic tests were run on a battery cycler (Neware, BTS 4000, China), and all potentiostatic tests were run on a potentiostat (VMP3, Biologic, France). Stripping and plating tests were run on the battery cycler at 2 mA cm^{-2} for 1 h with 10 cycles of 1 mA cm^{-2} for 1 h as preconditioning cycling. Tafel plots were run on the potentiostat with linear sweep voltammetry with a scan rate of 0.1 mV s^{-1} with a 200 mV overpotential over open current voltage (OCV ~ 0 V) *vs.* Li.

4.5. Material characterization

Scanning electron microscope (SEM) micrographs were obtained on Thermofisher Apreo 2S with a clean connect transfer cell. The SEM was equipped with a Trinity detection system (in-lens and in-column), ETD SE detectors. Energy dispersive X-ray spectroscopy (EDS) was performed on the same SEM using Thermofisher ultradry silicon drift detectors.

Titration gas chromatography (TGC) was performed with gas chromatographer (GC) (Agilent 8890) with a 250 μL sample loop running through thermal conductivity detectors, TCD, using N_2 as the carrier gas. The GC was fitted with Hayesep Q and a Molsieve 5A columns. The extracted postmortem delithiated cycled electrodes were sealed in a glass vial under argon, Ar, with a septum seal. Using a syringe, the sealed vial reacted with 2 ml of DI water. The resulting hydrogen, H_2, evolved from the reaction mixed with Ar was sampled using a gas tight syringe (Hamilton, USA). The H_2 evolved was diluted with N_2, in a ratio of 0.25 ml of gas sampled to 5 ml of N_2. This mixture was injected into the sample loop of the GC, with N_2 purged through the sample loop and TCDs between runs. To correlate the area under the peak in the chromatograph with a Li weight, a calibration curve was developed. This involved sealing multiple weights (0.25 mg to 3 mg) of Li in an Ar glovebox and measuring the peak areas of H_2 in the chromatograms. The correlation between unreacted metallic Li and H_2 arises from the reaction between Li and water: $2Li + 2H_2O \rightarrow 2LiOH + H_2$. Once obtaining the amount of metallic Li, the amount of Li trapped in the SEI was calculated from the mass balance:

$$\text{Total inactive Li} = \text{SEI-Li} + \text{Metallic Li from TGC}$$

In detail, the total amount of Li plated was first determined from the applied charge (in mAh). After the first stripping cycle, the irreversible Li loss was calculated from the coulombic efficiency. Using Faraday constant, both values were then converted from ampere-hour to milligrams of Li following the conversion:

$$1\text{C} = 1\,\text{A} \times \text{s} = 1 \times \frac{1}{3600}\,\text{h} = \frac{1}{3600}\,\text{Ah}$$

$$1\text{C} = 6.25 \times 10^{18}\ \text{e}^- = 1.038 \times 10^{-5}\ \text{mole}^-$$

$$\text{Li}^+ + \text{e}^- \rightleftharpoons \text{Li}$$

$$1\ \text{mAh} = 3.7368 \times 10^{-5}\ \text{mol Li} = 0.2594\ \text{mg Li}$$

Post-mortem XPS was conducted by plating Li on the various electrode materials at the same rate as the electrochemical tests, after which 10 cycles of plating and stripping were performed at the same 2 mAh cm^{-2} to build an SEI layer. The cells were then decrimped in an Ar glovebox after which they were transferred to the XPS to be sputtered. The XPS used was Thermo Scientific Nexsa G2 using Avantage with a monochromatic Al Kα X-rays (1486.6 eV). Depth profiling was performed using an Ar sputter gun with 60 s of sputtering per run.

Conflicts of interest

There are no conflicts to declare.

Data availability

All data supporting this articleare provided within the manuscript and supplementary information (SI). Supplementary information: SEM images, titration gas chromatograph, XPS spectra, and electrochemical measurements. See DOI: https://doi.org/10.1039/d5eb00196j.

Additional data or materials used in this study are available from the corresponding author upon request.

Acknowledgements

This work was financially supported by the National Science Foundation (2427203) and Cornell University. The authors acknowledge the Materials Characterization Core (MCC) at Drexel University and the Cornell Center for Materials Research (CCMR) for the use characterization facilities.

References

1 M. Armand and J.-M. Tarascon, *Nature*, 2008, **451**, 652.
2 J.-M. Tarascon, *Nat. Chem.*, 2010, **2**, 510.
3 J. B. Goodenough and Y. Kim, *Chem. Mater.*, 2010, **22**, 587.
4 D. Lin, Y. Liu and Y. Cui, *Nat. Nanotechnol.*, 2017, **12**, 194.
5 C.-X. Bi, L.-P. Hou, Z. Li, M. Zhao, X.-Q. Zhang, B.-Q. Li, Q. Zhang and J.-Q. Huang, *Energy Mater. Adv.*, 2023, **4**, 0010.
6 L.-P. Hou, X.-Q. Zhang, B.-Q. Li and Q. Zhang, *Mater. Today*, 2021, **45**, 62.

7 T. Yim, R. Pereira, N. Cardoza and V. Kalra, *ACS Appl. Energy Mater.*, 2023, **6**, 12326.
8 C. Fang, X. Wang and Y. S. Meng, *TRECHEM*, 2019, **1**, 152.
9 I. Yoshimatsu, T. Hirai and J. Yamaki, *J. Electrochem. Soc.*, 1988, **135**, 2422.
10 M. S. Whittingham, *Proc. IEEE*, 2012, **100**, 1518.
11 D. Lu, Y. Shao, T. Lozano, W. D. Bennett, G. L. Graff, B. Polzin, J. Zhang, M. H. Engelhard, N. T. Saenz, W. A. Henderson, P. Bhattacharya, J. Liu and J. Xiao, *Adv. Energy Mater.*, 2015, **5**, 1400993.
12 T. M. Hagos, T. T. Hagos, H. K. Bezabh, G. B. Berhe, L. H. Abrha, S.-F. Chiu, C.-J. Huang, W.-N. Su, H. Dai and B. J. Hwang, *ACS Appl. Energy Mater.*, 2020, **3**, 10722.
13 T. T. Hagos, B. Thirumalraj, C.-J. Huang, L. H. Abrha, T. M. Hagos, G. B. Berhe, H. K. Bezabh, J. Cherng, S.-F. Chiu, W.-N. Su and B.-J. Hwang, *ACS Appl. Mater. Interfaces*, 2019, **11**, 9955.
14 X. Bian, Y. Gao, Q. Fu, S. Indris, Y. Ju, Y. Meng, F. Du, N. Bramnik, H. Ehrenberg and Y. Wei, *J. Mater. Chem. A*, 2017, **5**, 600.
15 S. Jiao, J. Zheng, Q. Li, X. Li, M. H. Engelhard, R. Cao, J.-G. Zhang and W. Xu, *Joule*, 2018, **2**, 110.
16 J. Chen, J. Xiang, X. Chen, L. Yuan, Z. Li and Y. Huang, *Energy Storage Mater.*, 2020, **30**, 179.
17 J. Zheng, P. Yan, D. Mei, M. H. Engelhard, S. S. Cartmell, B. J. Polzin, C. Wang, J.-G. Zhang and W. Xu, *Adv. Energy Mater.*, 2016, **6**, 1502151.
18 N. A. Sahalie, Z. T. Wondimkun, W.-N. Su, M. A. Weret, F. W. Fenta, G. B. Berhe, C.-J. Huang, Y.-C. Hsu and B. J. Hwang, *ACS Appl. Energy Mater.*, 2020, **3**, 7666.
19 Z. T. Wondimkun, W. A. Tegegne, J. Shi-Kai, C.-J. Huang, N. A. Sahalie, M. A. Weret, J.-Y. Hsu, P.-L. Hsieh, Y.-S. Huang, S.-H. Wu, W.-N. Su and B. J. Hwang, *Energy Storage Mater.*, 2021, **35**, 334.
20 A. A. Assegie, J.-H. Cheng, L.-M. Kuo, W.-N. Su and B.-J. Hwang, *Nanoscale*, 2018, **10**, 6125.
21 A. A. Assegie, C.-C. Chung, M.-C. Tsai, W.-N. Su, C.-W. Chen and B.-J. Hwang, *Nanoscale*, 2019, **11**, 2710.
22 X. Wang, Y. He, S. Tu, L. Fu, Z. Chen, S. Liu, Z. Cai, L. Wang, X. He and Y. Sun, *Energy Storage Mater.*, 2022, **49**, 135.
23 K. Yan, Z. Lu, H.-W. Lee, F. Xiong, P.-C. Hsu, Y. Li, J. Zhao, S. Chu and Y. Cui, *Nat. Energy*, 2016, **1**, 1.
24 Y. Li, M. Bu, C. Mu and C. Yang, *Mater. Lett.*, 2024, **355**, 135449.
25 Q. Li, S. Zhu and Y. Lu, *Adv. Funct. Mater.*, 2017, **27**, 1606422.
26 Y. Chen, A. Elangovan, D. Zeng, Y. Zhang, H. Ke, J. Li, Y. Sun and H. Cheng, *Adv. Funct. Mater.*, 2020, **30**, 1906444.
27 M. Xie, X. Sun, C. Zhou, A. S. Cavanagh, H. Sun, T. Hu, G. Wang, J. Lian and S. M. George, *J. Electrochem. Soc.*, 2015, **162**, A974.
28 Enhancing lithium and sodium storage properties of TiO_2(B) nanobelts by doping with nickel and zinc.
29 F. Dou, Y. Weng, G. Chen, L. Shi, H. Liu and D. Zhang, *Chem. Eng. J.*, 2020, **387**, 124106.
30 Y. Nan, S. Li, B. Li and S. Yang, *Nanoscale*, 2019, **11**, 2194.
31 J. W. Kang, J. H. Choi, J.-K. Lee and Y. C. Kang, *J. Mater. Chem. A*, 2024, **12**, 7670.
32 Y. Li, S. Li, J. Cui, J. Yan, H. H. Tan, J. Liu and Y. Wu, *Nanoscale Adv.*, 2022, **4**, 4639.
33 Y. Wang, X. Xian, Y. Wang, Y. Guo and D. Xiao, *New J. Chem.*, 2024, **48**, 6462.
34 K. G. Reeves, J. Ma, M. Fukunishi, M. Salanne, S. Komaba and D. Dambournet, *ACS Appl. Energy Mater.*, 2018, **1**, 2078.
35 M. Shirpour, J. Cabana and M. Doeff, *Chem. Mater.*, 2014, **26**, 2502.
36 Layered Lepidocrocite Type Structure Isolated by Revisiting the Sol–Gel Chemistry of Anatase TiO_2: A New Anode Material for Batteries | Chemistry of Materials.
37 H. O. Badr, V. Natu, Ș Neațu, F. Neațu, A. Kuncser, A. M. Rostas, M. Racey, M. W. Barsoum and M. Florea, *Matter*, 2023, **6**, 2853.
38 L. Wang, H. O. Badr, Y. Yang, J. H. Cope, E. Ma, J. Ouyang, L. Yuan, Z. Li, Z. Liu, M. W. Barsoum and W. Shi, *Chem. Eng. J.*, 2023, **474**, 145635.
39 K. Sudhakar, T. Kono, T. El-Melegy, H. Badr, P. M. Laxmeesha, K. Montazeri, A. Semisalova, M. Farle, U. Wiedwald and M. W. Barsoum, *J. Magn. Magn. Mater.*, 2023, **582**, 170986.
40 N. A. Cardoza, H. O. Badr, R. Pereira, M. W. Barsoum and V. Kalra, *ACS Appl. Mater. Interfaces*, 2023, **15**, 50973–50980.
41 G. R. Schwenk, A. D. Walter, H. O. Badr, M. Q. Hassig, T. Kono, F. Lagunas, K. Montazeri and M. W. Barsoum, *Ceram. Int.*, 2023, **49**, 40001.
42 S. E. Holmes, F. Liu, W. Zhang, P. Sayavong, S. T. Oyakhire and Y. Cui, *ACS Appl. Mater. Interfaces*, 2022, **14**, 53736.
43 M. Airoldi, J. A. Berrocal, I. Gunkel and U. Steiner, *RSC Appl. Polym.*, 2025, **3**, 278.
44 X. Fan, Y. Li, C. Luo, S. Luo, B. Huang, S. Liu and W. Sun, *Electrochim. Acta*, 2023, **464**, 142896.
45 T. Xu, L. Hou, C. Yan, J. Hou, B. Tian, H. Yuan, D. Kong, H. Wang, X. Li, Y. Wang and G. Zhang, *Scr. Mater.*, 2023, **229**, 115352.
46 H. Chen, A. Pei, J. Wan, D. Lin, R. Vilá, H. Wang, D. Mackanic, H.-G. Steinrück, W. Huang, Y. Li, A. Yang, J. Xie, Y. Wu, H. Wang and Y. Cui, *Joule*, 2020, **4**, 938.
47 Poor Stability of Li_2CO_3 in the Solid Electrolyte Interphase of a Lithium–Metal Anode Revealed by Cryo–Electron Microscopy – Han – 2021 – Advanced Materials – Wiley Online Library.
48 Y. Liu, X. Xu, M. Sadd, O. O. Kapitanova, V. A. Krivchenko, J. Ban, J. Wang, X. Jiao, Z. Song, J. Song, S. Xiong and A. Matic, *Adv. Sci.*, 2021, **8**, 2003301.
49 A. Pei, G. Zheng, F. Shi, Y. Li and Y. Cui, *Nano Lett.*, 2017, **17**, 1132.
50 Y. Liu, X. Xu, M. Sadd, O. O. Kapitanova, V. A. Krivchenko, J. Ban, J. Wang, X. Jiao, Z. Song, J. Song, S. Xiong and A. Matic, *Adv. Sci.*, 2021, **8**, 2003301.
51 D. Grujicic and B. Pesic, *Electrochim. Acta*, 2002, **47**, 2901.
52 B. Scharifker and G. Hills, *Electrochim. Acta*, 1983, **28**, 879.

53 E. Navarrete, C. Heyser, R. Henríquez, R. Schrebler, R. Córdova and E. Muñoz, *J. Electroanal. Chem.*, 2014, **727**, 39.
54 C. Fang, J. Li, M. Zhang, Y. Zhang, F. Yang, J. Z. Lee, M.-H. Lee, J. Alvarado, M. A. Schroeder, Y. Yang, B. Lu, N. Williams, M. Ceja, L. Yang, M. Cai, J. Gu, K. Xu, X. Wang and Y. S. Meng, *Nature*, 2019, **572**, 511.
55 S. E. Holmes, F. Liu, W. Zhang, P. Sayavong, S. T. Oyakhire and Y. Cui, *ACS Appl. Mater. Interfaces*, 2022, **14**, 53736.
56 A. Dutta, K. Matsushita and Y. Kubo, Adv. Sci., 2404245.
57 S. Xiong, K. Xie, Y. Diao and X. Hong, *Electrochim. Acta*, 2012, **83**, 78.
58 S. Lorger, K. Narita, R. Usiskin and J. Maier, *Chem. Commun.*, 2021, **57**, 6503.
59 L. Wang, H. O. Badr, Y. Yang, J. H. Cope, E. Ma, J. Ouyang, L. Yuan, Z. Li, Z. Liu, M. W. Barsoum and W. Shi, *Chem. Eng. J.*, 2023, **474**, 145635.
60 N. Cardoza, *BioRender*, 2026, https://BioRender.com/sxw7jat.